Article:

Tornquist, F., Bigg, G.R. and Bryant, R.G. orcid.org/0000-0001-7943-4781 (2024) Climate drivers of phytoplankton production along the Chilean coast. Journal of Marine Systems, 246. 104013. ISSN 0924-7963

https://doi.org/10.1016/j.jmarsys.2024.104013

Journal of Marine Systems 246 (2024) 104013

Contents lists available at ScienceDirect

Journal of Marine Systems

journal homepage: www.elsevier.com/locate/jmarsys

Climate drivers of phytoplankton production along the Chilean coast

Felipe Tornquist [*], Grant R. Bigg, Robert G. Bryant

Department of Geography, University of Sheffield, Winter Street, Sheffield S10 2TN, UK

ARTICLE INFO

Keywords:
CCA
Chl
SPSA
ENSO
SST
Southerly winds

ABSTRACT

The west coast of South America is known for its high primary productivity. The level of phytoplankton can be measured through satellite images that detect chlorophyll (Chl), which is dependent on several oceanographic and meteorological parameters. Climate drivers such as El Niño Southern Oscillation (ENSO) and the Southeast Pacific Subtropical Anticyclone (SPSA) affect these parameters and, consequently, the phytoplankton. The objective of this study was to identify the impact of ENSO on SPSA, climate variables, and phytoplankton patterns. Composites were created using the years selected with either strongly positive or negative ENSO to understand their influence on different parameters. To create the Chl composite, it was necessary to extend it using Canonical Correlation Analysis (CCA) based on the sea surface temperature (SST) pattern. The study concludes that ENSO has a noticeable impact on Chl, mainly in the Southern Zone during the warm season. This is driven by the expansion of SPSA to the South, which increases the sea level pressure (SLP) in that region. However, predicting the Chl concentration has a high degree of uncertainty due to its complexity.

1. Introduction

The Southeast Pacific Subtropical Anticyclone (SPSA) is the main atmospheric circulation component in the South Pacific Ocean, affecting from 0° to 42°S near the South American coast (Aguirre et al., 2021). The SPSA is characterised by a high-pressure system centred at 30°S, and it exhibits seasonal movement, impacting the coasts of Ecuador, Peru, and the northern to central part of the Chilean coast (Ancapichun and Garcés-Vargas, 2015). This climate driver leads to generally stable weather conditions with significant alongshore and equatorwards winds from 5°N to 40°S. These winds induce coastal upwelling, enriching surface waters with nutrients from deeper ocean layers and lowering the sea surface temperature (SST; Thiel et al., 2007). These conditions are enhanced by the meridionally oriented coastline (Thiel et al., 2007) and the presence of the Andes, which restrain the SPSA and block atmospheric frontal systems from the southwest (Barrett et al., 2009; Schulz et al., 2012). This distinctive setting makes this region one of the most productive oceanic zones, featuring a significant phytoplankton concentration that can be easily measured by satellite using Chlorophyll-α (Chl; Mogollón and Calil, 2017; Vergara et al., 2017; Tornquist et al., 2024).

The SPSA undergoes seasonal, interannual and interdecadal cycles, leading to fluctuations in wind direction (meridional winds VW and zonal winds UW) and intensity (Ancapichun and Garcés-Vargas, 2015). During the austral summer, the SPSA's core migrates southwards to 35°S, resulting in southerly winds that prevail up to 42°S. However, it retreats towards the Equator in the austral winter (Fig. 1). This seasonal movement creates a significant wind variability between 35° to 42°S (Rahn, 2012; Ancapichun and Garcés-Vargas, 2015; Aguirre et al., 2021). Consequently, the Central Zone of the Chilean coast experiences cold fronts from the south during the winter, producing westerly winds, intense precipitation rates (PR) episodes and downwelling conditions (Fig. 1). Simultaneously, the region from 40 to 42°S experiences dry summers (Ancapichun and Garcés-Vargas, 2015; Rahn, 2012; Quintana and Aceituno, 2011). The winds in the 18° to 28°S section maintain their alongshore direction, but are weakened (Ancapichun & Garcés, 2015; Rahn, 2012; Aguirre et al., 2021). On an interannual scale, SPSA variability is driven by the El Niño Southern Oscillation (ENSO) and Antarctic Oscillation (AAO), altering the South Pacific dipole (Ancapichun and Garcés-Vargas, 2015; Garreaud et al., 2020; Garreaud and Muñoz, 2005).

The ENSO is a recurring disruption in the ocean-atmosphere system, typically occurring every 2–7-years. This phenomenon alters the sea level pressure (SLP) differences between the western and eastern Pacific coasts, thereby modifying the Walker atmospheric circulation over the equatorial Pacific Ocean (Bigg, 2003; CONAMA, 2008). During El Niño conditions, weakened or altered trade winds lead to decreased sea levels in the western Pacific, flattening the thermocline (Bigg, 2003). This

---

[*] Corresponding author.
E-mail addresses: Felipetornquist@hotmail.com (F. Tornquist), grant.bigg@sheffield.ac.uk (G.R. Bigg), r.g.bryant@sheffield.ac.uk (R.G. Bryant).

https://doi.org/10.1016/j.jmarsys.2024.104013
Received 15 February 2024; Received in revised form 10 September 2024; Accepted 12 September 2024

results in warmer waters along the eastern coast of South America, as the relaxed equatorial current allows warm water propagated eastwards by Kelvin waves. Consequently, the entire Chilean coast can experience temperature increases ranging from 1 to 4 °C (Ancapichun and Garcés-Vargas, 2015; Schollaert Uz et al., 2017; Echevin et al., 2014; Gómez et al., 2012; Saldías et al., 2016).

El Niño's impact extends beyond SST. The warming induces low-pressure systems in the east Pacific mid-latitudes, leading to intensified PR and reduced longshore winds in the region (Cordero et al., 2019; Garreaud et al., 2020, Vicente-Serrano et al., 2017). These conditions cause a deeper thermocline and weaker upwelling winds, which in turn lower nutrient levels and a decrease primary production in the Central Zone (Mogollón and Calil, 2017).

Despite the typical strengthening of coastal winds from 10 N° to 25°S during El Niño events, which usually enhances upwelling (Enfield, 1981; Kessler, 2006; Chamorro et al., 2018; Huyer et al., 1987), the upwelling during El Niño tends to bring warmer and less nutrient-rich waters to the surface. This is due to the deepening of the thermocline and nutricline caused by the downwelling coastal waves (Barber & Chavez, 1983; Calienes, 2014; Echevin et al., 2014; Graco et al., 2016; Espinoza-Morriberón et al., 2017).

Conversely, La Niña, the cold phase of ENSO, introduces a negative SST anomaly of approximately 1–2 °C in the Equatorial Pacific (NOAA, 2019). This phase intensifies the upwelling process through stronger easterly winds in the Equatorial Pacific, raising sea level in the western Pacific (Bigg, 2003). La Niña increases the nutrient supply by upwelling waters from a shallower thermocline and nutricline (Bigg, 2003; CONAMA, 2008). Simultaneously, it reinforces the SPSA effect, amplifying the pressure difference in the South Pacific dipole. This leads to drier winters in the mid-latitudes (Garreaud et al., 2020) but also weakens the coastal winds from 10 N° to 25°S (Enfield, 1981; Kessler, 2006; Chamorro et al., 2018; Huyer et al., 1987).

In a previous study (Tornquist et al., 2024), we examined the impact of physical parameters such as PR, SST, UW, and VW on phytoplankton behaviour along the Chilean coast, specifically noting the differences between each Zone (Northern, Central and South). We observed that this behaviour is influenced by the SPSA annual pattern, which creates upwelling conditions, and shelf width. Our study also considered the nutrient input from precipitation and rivers, concluding that the upwelling mechanism driven by the SPSA is the most significant factor in phytoplankton fertilization.

However, we did not explicitly consider the influence of climate drivers such as ENSO on the SPSA. Given the substantial impact of these climate drivers on physical parameters and, consequently, phytoplankton fluctuations, a more comprehensive understanding is required (Vergara et al., 2017; Echevin et al., 2014; Ancapichun and Garcés-Vargas, 2015). Yet, quantifying these climate driver impacts is complicated by the range of time and space scales at which they operate. Addressing this challenge necessitates a thorough comprehension of how these drivers contribute to observed patterns in these key meteorological variables across appropriate space and time scales (Von Storch and Zwiers, 1999). Therefore, establishing a baseline understanding of phytoplankton status in the study region is imperative. Although data are available from 1979 onwards, continuous Chl data is only accessible from 1997, which necessitates extension through statistical methods (Schollaert Uz et al., 2017).

This paper aims to build directly on the work of Tornquist et al. (2024) and determine the effects of ENSO on phytoplankton dynamics in the Chilean coastal region. Its main objectives are to i) extend the Chl record from 1979 to 2018 using Canonical Correlations Analysis (CCA), ii) develop composite maps using only the highest intensity years of ENSO in both phases in order to detect possible changes of the key physical parameters and Chl, and iii) determine the ENSO effect on SPSA and Chl patterns.

2. Material and methods

2.1. Study area

The research conducted in this study is focused on the Chilean coast.

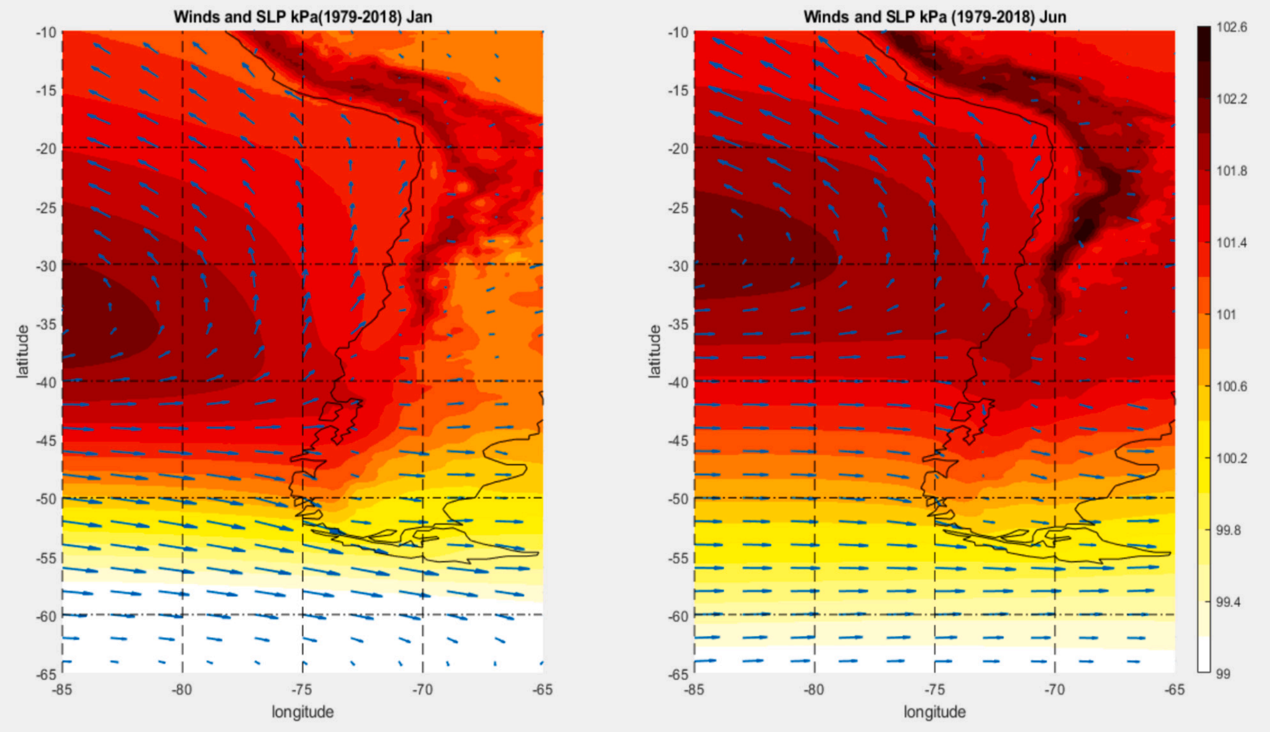

Fig. 1. The monthly averaged sea level pressure (SLP) and winds from 1979 to 2018 were calculated using the ERA5 dataset. The panels show how the high-pressure centre varies from January (Left) to July (right) and how these affect the wind direction.

The coast has been divided into three main zones, and these are further divided into three subsections. The criteria for defining these zones are based on the work of Tornquist et al. (2024), with one exception: the Central Zone has been split into three subsections instead of four to provide a larger area for observing patterns with greater clarity (Fig. 2). The mechanism of each zone was studied in detail in Tornquist (2023), and some key elements are mentioned in Tornquist et al. (2024). The mechanism specifics of each Zone were studied in detail in Tornquist (2023) and some key elements are mentioned in Tornquist et al. (2024) and Tornquist (2023).

2.2. Data selection

Composite maps are a technique that helps to determine the impact of a climate driver on various parameters. This is done by calculating the average of each variable, using only the dates when the climate driver was more intense in its positive or negative phase (Von Storch and Zwiers, 1999). The Composite maps' grid was built over the following coordinates 10° to 65°S and 85°W to 65°S. The area of interest was expanded to facilitate analysis of higher latitude zones to incorporate possible patterns connecting the Chilean coast with the open ocean, Peru and the Drake Passage.

The variables that were examined in these composites are those that have been affected by ENSO and SPSA variations, such as PR, SST, UW, VW and SLP (Thiel et al., 2007; Ancapichun and Garcés-Vargas, 2015; Rahn, 2012; Aguirre et al., 2021; Tornquist et al., 2024). Meanwhile, the phytoplankton levels were estimated using the Chl concentration obtained through remote sensing (Tornquist et al., 2024).

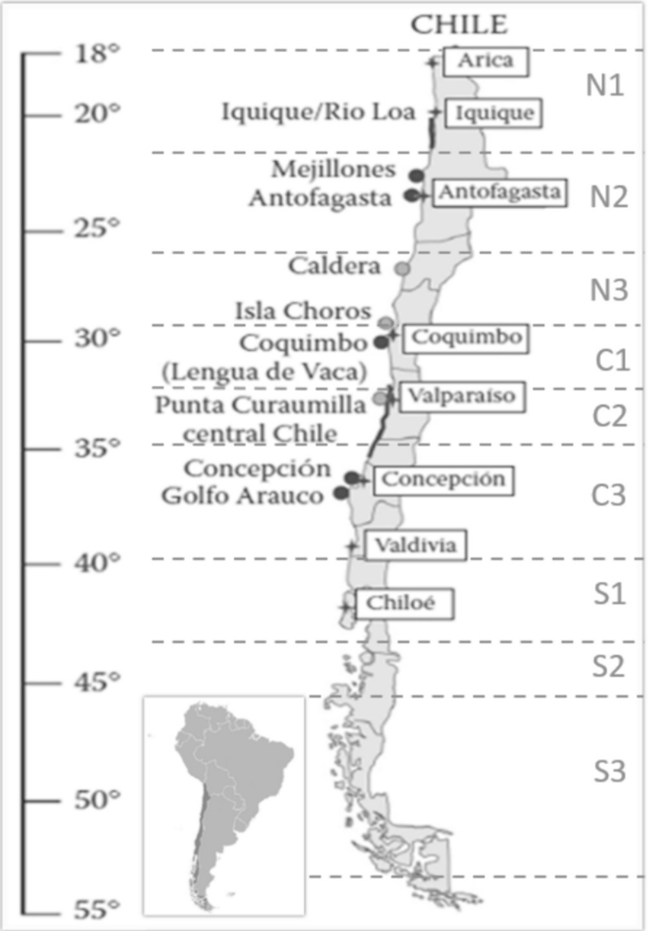

Fig. 2. Chilean map delimiting the zones (N: North, C: Central and S: South) of study and its subsections.

The physical parameter data used in this study are derived from The European Centre for Medium-Range Weather Forecast (ECMWF) model known as ERA5 (ECMWF ReAnalysis fifth version). ERA5 is a global reanalysis system that integrates satellite and observational data, providing improved physical parameter datasets from 1979 onwards, with a spatial resolution of 0.25° x 0.25° (C3S, 2021; https://cds.climate.copernicus.eu/cdsapp; Table 1). This version, introduced in 2016, includes several key improvements, offering a better global balance of precipitation and more consistent ice patterns than ERA-interim and Tropical Rainfall Measuring Mission (TRMM: Hersbach et al., 2020; Tang et al., 2020). However, while SST is used as a forcing in the simulations, ERA5 still faces challenges in accurately capturing rainfall quantities in arid regions (Tang et al., 2020).

The Chl data were obtained from GES DISC (Goddard Earth Sciences Data and Information Services Centre) Interactive Online Visualization and Analysis Infrastructure (GIOVANNI; https://giovanni. gsfc.nasa.gov/giovanni/) using Moderate Resolution Imaging Spectroradiometer MODIS-aqua data exclusively from 2003 to 2018 (Table 1). Sea-Viewing Wide Field-of-View Sensor (SeaWiFS) data from 1997 to 2010 was not used to extend the Chl time scale because using mixed sensors would produce considerable errors due to their spectra bandwidth differences. Additionally, their spatial and temporal resolution do not match, generating gaps that are not straightforward to interpolate within (Franz et al., 2005). Although there is now a Chl dataset that includes both sensors' data in Copernicus, this was unavailable during the development of this research.

A range of indices are commonly used to measure the intensity of ENSO and SPSA. Given ENSO's complexity, various indices are necessary to gauge its impact. This paper focuses on the ENSO index measured in the 3.4 region. This index is determined by averaging SST anomalies over a thirty-year base period in the Central Pacific (Vicente-Serrano et al., 2017). The ENSO 3.4 region index is widely recognised for defining El Niño and La Niña events (Trenberth, 2020) and has been extensively utilised in research and by institutions such as the Chilean Meteorological Directorate (DMC) and in studies by Ancapichun and Garcés-Vargas (2015). On the other hand, the SPSA index is calculated by normalising SLP anomalies from eight meteorological stations between the Northern and Central zones of Chile. Then, the SLP anomalies are compressed into one using the first Empirical Orthogonal Function (EOF; Quintana and Aceituno, 2011). The National Oceanic and Atmospheric Administration (NOAA) estimates the ENSO index (see https://origin.cpc.ncep.noaa.gov/products/analysis_monitoring/ENSOstuff/ONI_change.shtml), while the SPSA is calculated by the DMC based on Quintana and Aceituno's (2011) methodology. We were kindly provided with data for this index by Vicencio (2021).

2.3. Chl time series reconstruction using CCA

Characterising Chl variability adequately can be difficult due to the complex relationship that exists between Chl and a wide range of variables (Schollaert Uz et al., 2017; Tornquist et al., 2024). However, CCA has been proven to be a viable and adaptable analysis tool for these types of data (Schollaert Uz et al., 2017). CCA analysis determines the number of relationships between two or three sets of variables, known as *predictors* and *predictands,* and projects them in a new coordinate system. This is achieved by using the optimal correlation between variables through EOF analysis. In this way, CCA maximised the correlation (called Canonical correlation, Rc) between the covariance of the predictor and the predictand's EOF (Variates), which is made by a Singular Value Decomposition (Schollaert Uz et al., 2017; Barnett and Preisendorfer, 1987; Taylor et al., 2013). When the predictand and predictor have comparable space-time fields, and a significant correlation is established, CCA can forecast the predictand to a time gap based on the predictor behaviour using the best correlation possible. CCA is an innovative approach for environmental data reconstruction. Schollaert Uz et al. (2017) have carried out successful Chl prediction using this

Table 1
Parameters used in this research as core data-sets in the composite analysis and Chl reconstruction.

Parameter	Unit	Source	Temp res.	Spatial res.	Date begins	End Date
Chl	mg m^{-3}	MODIS-Aqua	Monthly	0.04° x 0.04°	04/07/2002	31/06/2018
SST	K	ERA5	Monthly	0.25°x 0.25°	01/01/1979	31/06/2018
Total Precipitation	M	ERA5	Monthly	0.25°x 0.25°	01/01/1979	31/06/2018
Westerly Wind (10 m)	m s^{-1}	ERA5	Monthly	0.25°x 0.25°	01/01/1979	31/06/2018
Southerly Wind (10 m)	m s^{-0}	ERA4	Monthly	0.25°x 0.25°	31/12/1978	31/06/2018
Sea Level Pressure	Pa	ERA5	Monthly	0.25°x 0.25°	01/01/1979	31/06/2018

approach. Despite known uncertainty in the outputs, this approach was deemed suitable to establish the general Chl pattern sought by this research. Prior to processing the Chl data, a pre-treatment is normally required to fill apparent gaps due to excessive cloudiness (Gómez et al., 2017). The Data Interpolating Empirical Orthogonal Functions (DINEOF) method was used to address this issue (Echevin et al., 2014). The Sinkr R package provided the EOF and DINEOF routines (Taylor, 2017), while the CCA code was written by Taylor (2012). The mathematical details for CCA and EOF can be found in Wilks (2011), and for DINEOF in Beckers and Rixen (2003). It is important to note that all variables must be normalised for these techniques to work properly (Schollaert Uz et al., 2017). The normalisation process involves subtracting the mean from each value and dividing by the standard deviation (SD). This process is carried out monthly for each grid point.

2.3.1. Generation of DINEOF and EOF outputs

Within the study region, a total of 553,891 data points, representing around 24 % of the Chl data, were found to be missing due to adverse weather conditions and clouds. This mainly affected S2 and S3 subsections from April to August (Fig. 2). To fill all data gaps, the DINEOF technique was employed, and errors were calculated using a cross-validation approach. Here, cross-validation randomly selected 1 % of the data (17,002 points) to check how effective each iteration was (Beckers and Rixen, 2003). This resulted in a final count of 22 EOFs after 169 iterations. The Root Mean Square (RMS) error stabilised at 0.829, which is deemed acceptable, given both the −3.3 to 3.6 range of Chl anomalies and a tolerance error of around 12 %.

To extend the Chl dataset from 1970 to 2002, variables VW and SST were tested, both of which were shown to be significantly correlated with the Chl in this region, according to Tornquist et al. (2024). However, since these two variables have a high correlation, they could not be used together (Barnett and Preisendorfer, 1987; Taylor et al., 2013). Therefore, a separate stage of EOF analysis was performed for these two variables and Chl in order to determine which could provide a better prediction; Fig. 3 shows the truncation and the cumulative explained variance. The selection was made using North's Rule-of-Thumb, as explained by Wilks (2011) and Barnett and Preisendorfer (1987).

In Fig. 3, it is evident that SST had the sharpest curve, indicating that it had well-defined patterns that required fewer EOFs to achieve a good approximation. In contrast, the Chl curve was shallow, indicating that it was less well represented by its EOFs because it has a high variation hard to predict. However, the Chl fulfilled the North's Rule-of-Thumb criteria first, requiring only twenty EOFs, but keeping only 55 % of the variance. SST required twenty-seven EOFS and explained 92 % of the variance, while VW needed nineteen EOFs and explained 89 % of the variance. The sensitivity of the Chl pattern was tested by examining its prediction with fewer (fifteen) and more (thirty) EOFs retained. The results showed that the variance explained was 50 % and 61 %, respectively. Thus, there were no significant differences in the Chl prediction. This indicates that the key elements that explain the Chl behaviour are already captured by the first fifteen EOFs.

2.3.2. The CCA procedure, and output generation

The aim of this analysis was to determine whether SST or VW is a better predictor of Chl. To achieve this the model employs a Training Mode. During this mode, CCA was performed over a shorter period (2003–2013), excluding a portion (2014–2018) of the Chl time-series (Taylor et al., 2013; Schollaert Uz et al., 2017). This model used the results from 2003 to 2013 to predict the Chl values from 2003 to 2018. Following this, a Full Mode was run over the 2003–2018 period to predict the Chl time series from 1979. To estimate the error in the Training Mode, the Ch prediction (2003–2018) was correlated with the Chl data (2003–2018) and the correlation R (do not confuse with Rc) per location was mapped (Fig. 4). The Mean Absolute Error (MAE) was also calculated, which is appropriate for data that has been normalised (Taylor et al., 2013). This procedure was also done with the test set only (2014–2018), where the Chl data was not used to feed the model.

Figure 4 shows that the most accurate prediction of the Chl was achieved using SST (Chl-SST), with an average R of 0.45 and MAE of 0.63, resulting in an overall 9.7 % error for the Full Mode. On the other hand, VW showed an average R of only 0.21. Chl-SST was also the best prediction during the Training Mode, but the average R decreased to 0.33 with an MAE of 0.72, leading to a higher error of 10.7 %. It is worth noting that Chl-VW exhibited a stronger correlation with the Chl in the

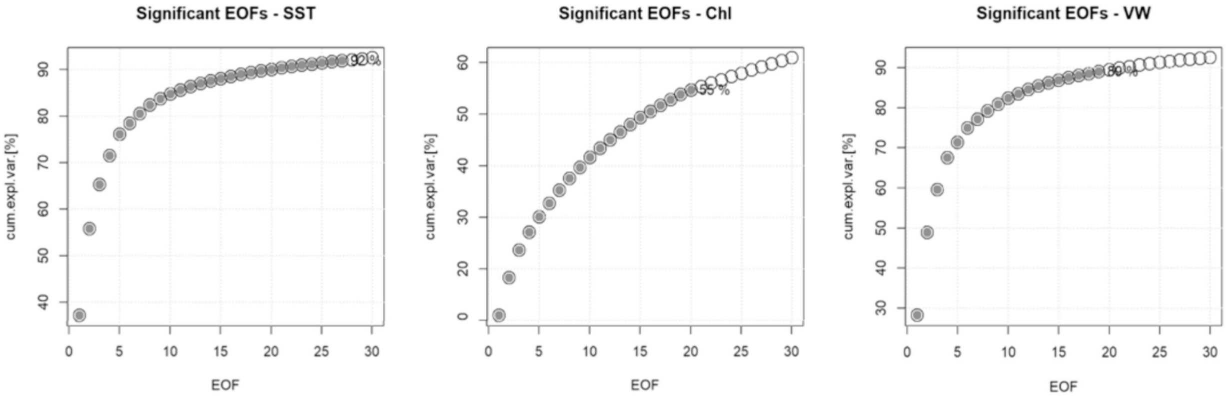

Fig. 3. The cumulative sum of the variance in the percentage of SST, Chl and VW. The grey points showed the temporal EOF selected in the construction. Note that The Y-axis, showing the cumulative explained variance, has a different scale for each graph.

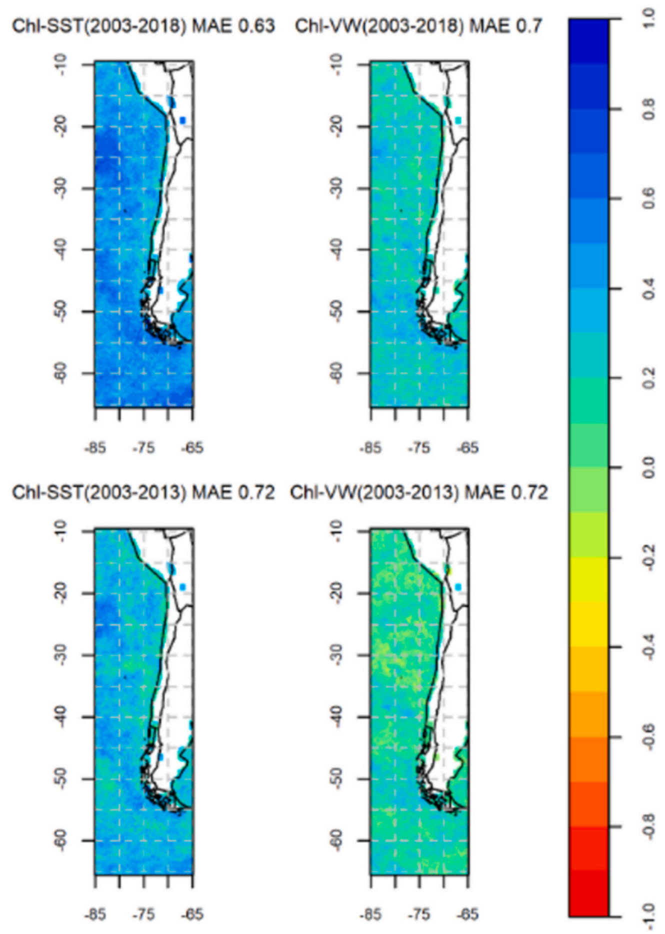

Fig. 4. Correlation R of the Chl vs the Chl predicted fields using SST and VW. The first row shows the CCA prediction using Full Chl data (2003–2018). The bottom row shows the Chl predicted over 2003–2018 years using the Training Mode (2003–2013) correlated with the Chl data (2003–2018).

Southern Zone coast, indicating a significant influence of the southerly winds when they are present. Although the relationship was weaker when the real data was missing, giving a MAE of 0.85 in the test set (2013–2018), the error remained relatively consistent due to the pattern-based approach of CCA.

Fourteen out of twenty CCA components (modes) were used to construct the SST and Chl Variates, with a Rc ranging from 0.89 to 0.45 in the Full Mode. In the Training Mode, sixteen modes out of twenty were required, with Rc ranging from 0.93 to 0.46 (Table 2). The Training Mode presented a higher Rc range due to its shorter period. The truncation of the modes was defined using the Pillai–Bartlett trace criteria (Friederichs and Hense, 2003; Taylor, 2012).

Spatial EOFs for the Chl time-series can be recreated using the CCA model based on the SST spatial EOF (Wilks, 2011; Barnett and Preisendorfer, 1987). These are shown in Figs. 5–6, which display the first 5 EOFs for both the Training and Full Modes, while Table 3 shows the results.

The Chl-SST prediction reproduced well the first three EOFs in the Training Mode, especially EOF 3 (Fig. 5, Table 3). However, the predicted EOFs did not follow the original EOF curves correctly over the period in which the data were not used to feed the model (2014–2018). Only EOFs 1–3, 9, 11, 14, 16 and 17 had an R above 0.5. The EOFs 4, 10, 13, 15, 18–20 were loosely followed, with an R below 0.4 (Table 3).

The Chl-SST prediction was able to reproduce the first three Chl EOFs with good accuracy in the Full Mode, especially for EOFs 2 and 3 (Fig. 6). Additionally, EOFs 7 and 14 were also well correlated with an R over 0.7 (Table 3, see Tornquist, 2023). For the other EOFs, their general tendency was matched with an R above 0.5, except for EOF 12, 19 and 20 (Table 3, see Tornquist, 2023). The main differences found were that all the predicted EOF curves had smoother behaviour than the originals, which presented a high variability.

Table 2
Rc for the modes using Chl-SST in the Full Mode and Training Mode, the underlined value indicates when it was truncated.

Mode	Full Mode	Training Mode
1	0.89	0.93
2	0.87	0.91
3	0.84	0.9
4	0.82	0.89
5	0.79	0.85
6	0.76	0.81
7	0.73	0.75
8	0.69	0.73
9	0.67	0.74
10	0.62	0.69
11	0.57	0.67
12	0.51	0.64
13	0.49	0.57
14	0.45	0.53
15	0.42	0.51
16	0.36	0.46
17	0.30	0.43
18	0.26	0.37
19	0.19	0.34
20	0.13	0.20

The Ch-SST Training Mode utilised sixteen CCA modes (Table 2) to describe the patterns of the first twenty Chl EOFs that account for 30.1 % of the variance (Table 3), with an R value of over 0.5. For the Full Mode, fourteen modes were needed to explain 34.1 % of the variance with an R value of over 0.6 (Table 3), while 14.2 % of the variance was explained with an R value between 0.5 and 0.6. This represents 48.3 % of the total Chl variance of 55 % that can be accounted. The Full Mode reconstruction was used for the subsequent analysis, and the error was likely to be similar to that of the Training Mode.

To summarise, the most accurate prediction was achieved using SST, with an average R-value of 0.45 and an MAE of 0.63 for the available data. However, for unknown data, these values were 0.33 and 0.72, respectively. This error is significant and can be attributed to excessive variation in Chl. Nevertheless, it is considered acceptable since only Chl anomalies beyond ±0.5 SD were taken into account in this composite analysis.

2.4. *Climate driver analysis and composite creation*

This analysis constructs composites using normalised Chl anomaly data from years with more intense ENSO activity. A complete Chl time-series was derived (a) for 1979 to 2003 using CCA based on SST (section 2.3), and (b) 2003 to 2018 from Chl measured by MODIS-aqua but using DINEOF to fill the gaps (section 2.3.1).

2.4.1. *Preliminary analysis of ENSO3.4 and SPSA*

Both indices were analysed using monthly and annual time windows (Fig. 7). The analysis revealed that ENSO exhibits a more consistent pattern with a variable 2–5-year periodicity but with a few exceptions. On the other hand, the SPSA index presented higher monthly variation, with a more negative trend in the mid-1980s and the first half of the 1990s. From 2000 to 2005, the behaviour of the SPSA was more neutral, while from 2006 onwards, it showed a positive tendency. This recent intensification was reported by Salvatteci et al. (2018) and Aguirre et al. (2021). ENSO showed a significant negative correlation with SPSA (p-value <0.01) on a yearly mean variation (-0.63), while the correlation was -0.39 on a monthly scale, likely due to the extreme variation in SPSA.

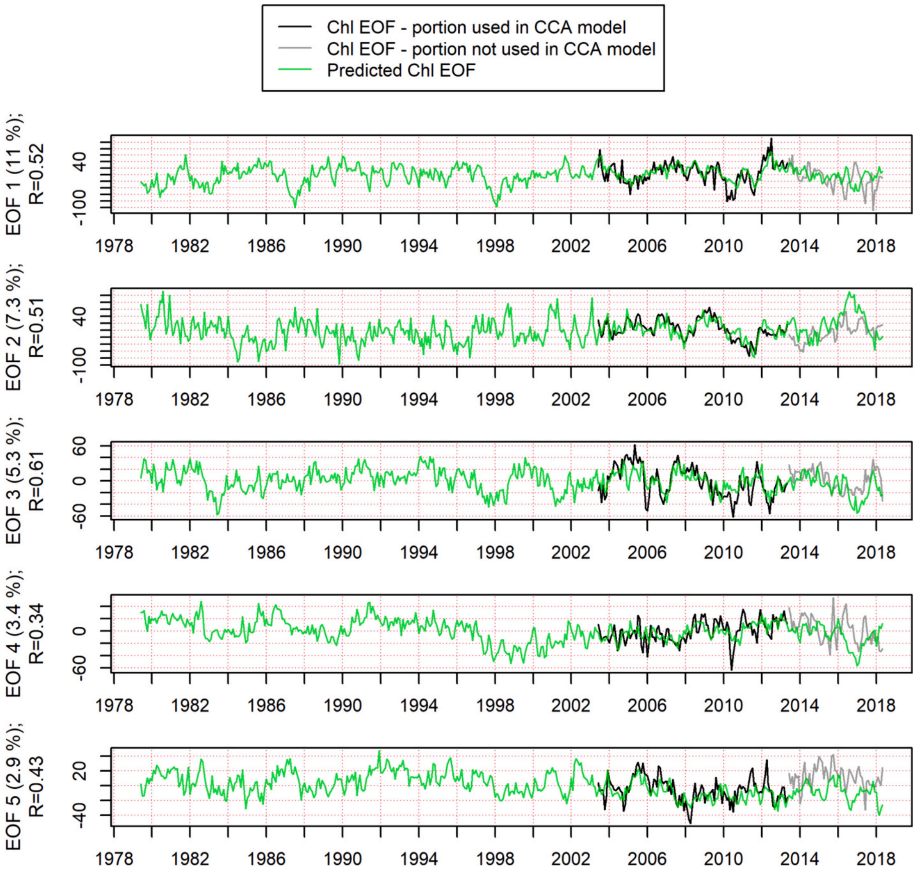

Fig. 5. CCA Chl EOF 1–5 prediction (1979–2018) using Chl-SST Training Mode (2003–2013). R indicates the correlation between the prediction and each real Chl EOF.

Due to its lower variability, the ENSO is more manageable than the SPSA in terms of accuracy for creating composites. As the ENSO is responsible for changing the SPSA's behaviour, we will only construct an ENSO composite. This will allow us to observe the ENSO's impact on the SPSA. Tornquist et al. (2024) examined the monthly spatial variability of Chl in each subsection and its correlation with the parameters listed in Table 1, excluding SLP. These variations are closely linked to the variation in the SPSA index.

2.4.2. *Creation of ENSO composites*

To determine the typical behaviour of each variable (Chl, SST, PR, UW, VW and SLP; Table 1), composite maps were created using the annual values during more intense ENSO events (e.g. as defined by Von Storch and Zwiers, 1999). The criteria for creating these composites were to (a) have the same minimum limit value for each cycle to enable similar intensities comparison between El Niño and La Niña and (b) try to keep the number of outliers constant.

Some adjustments to the time series were made before selecting the extreme years for the composite. A deeper analysis of the annual ENSO cycle revealed that strong El Niño events usually started with a significant rise in September, reaching a peak from November to January. The values for the following months tended to decrease until March or April, when the SST anomalies were close to 0. Therefore, we determined that to ensure the highest point in the ENSO cycle is in the middle of the sample, and that the composite data does not cross a typical ENSO cycle year the starting month of ENSO composites must be June. Considering these modifications, the minimum limit selected for ENSO cycles was an index value of ±1 (Fig. 8). There are thus four positive outliers (1981, 1991, 1997 and 2015) and five negative outliers (1988, 1998, 1999, 2007 and 2010).

3. Results

3.1. *Use of composites maps to understand phytoplankton dynamics in ENSO cycles*

In this section, we discuss the positive and negative ENSO Chl anomaly composites focusing on the coastal zone of Chile, with some exceptions. These composites were constructed using Chl data from MODIS-aqua from 2003 to 2018, and the data from 1979 to 2002 was extended using CCA based on the SST patterns (section 2.3). The ENSO composite construction was made using the years that had either extremely positive (El Niño) or negative (La Niña; section 2.4.2 and Fig. 8) events.

The El Niño Chl composite (Fig. 9.a) displayed positive Chl anomalies from September to May, with the highest peak from September to December. The Southern Zone, particularly S2 and S3, was the most affected area. This Chl increase extended from the coast to the open ocean sections. This was also linked with a Chl shift from September to May in the Drake Passage. Another area of significant Chl increments was observed in the N1-N2 subsections from October to December. In the same period, a Chl decline was observed in the Peruvian Zone. The Central Zone (C1-C3) did not show significant changes, apart from a decrease between January and April. However, C2 and C3 displayed a slight upsurge in Chl anomalies during the last month of that period.

During La Niña (Fig. 9.b), the positive Chl anomalies were not as substantial as they were during El Niño. In fact, the trend seemed to be more towards negative anomalies, with no anomalies exceeding±1 along the coast, which is unexpected. From June to October, there was a drop in the Chl concentration in the Northern and Central Zone. However, a slight local increase was observed in December in N1, N3, and C1. In the Southern Zone, S1 had a persistent positive anomaly for

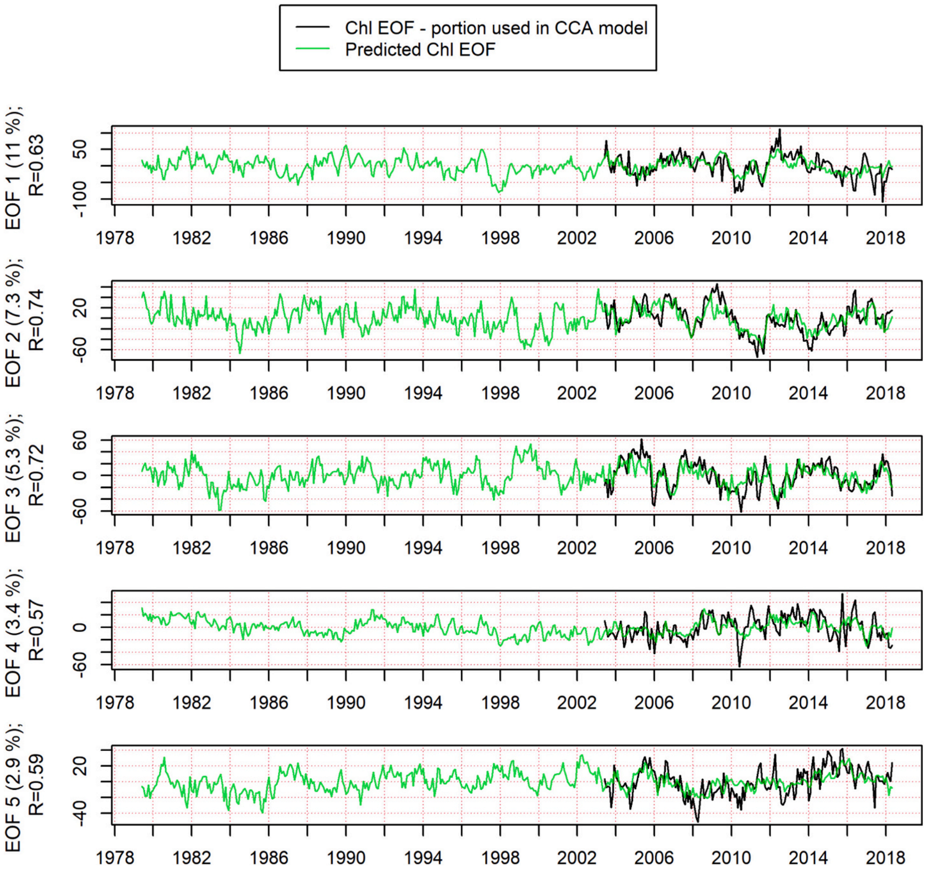

Fig. 6. CCA Chl-EOF 1–5 prediction (1979–2018) using Chl-SST Full Mode (2003–2018), R indicates the correlation between the prediction and each real Chl EOF.

Table 3
CCA Chl-EOF using Chl-SST Training (2003–2013) and Full Modes (2003–2018), R indicates the correlation between the prediction and each real Chl EOF, and the variance explained for each Chl EOF.

EOF	Var exp	Training Mode R	Full Mode R
1	11.0 %	0.52	0.63
2	7.3 %	0.51	0.74
3	5.3 %	0.61	0.72
4	3.4 %	0.34	0.57
5	2.9 %	0.43	0.59
6	2.7 %	0.43	0.57
7	2.6 %	0.46	0.72
8	2.4 %	0.49	0.66
9	2.2 %	0.52	0.63
10	2.0 %	0.32	0.5
11	1.9 %	0.56	0.62
12	1.7 %	0.45	0.48
13	1.5 %	0.36	0.55
14	1.4 %	0.5	0.7
15	1.3 %	0.31	0.55
16	1.2 %	0.55	0.6
17	1.2 %	0.51	0.6
18	1.1 %	0.37	0.5
19	1.0 %	0.16	0.3
20	0.9 %	0.27	0.41

almost the entire year, reaching the whole section in July–August. From December to May, there was a slight reduction in S2-S3.

3.2. *Use of physical composites to understand parameter behaviour in ENSO cycles*

The composites for the physical variables, including SST, PR, VW and UW, were created using the same procedure as the Chl composite (not shown, see Tornquist, 2023). Figs. 10 and 11 provide a summary of these variables, only displaying when their anomalies were over ±1.0 in conjunction with the Chl composite in the background. This was done in order to identify any changes in the key physical parameters that could explain the Chl variations. The correlations presented in Table 4 were used to assess the impact of these parameters on the Chl anomalies. These correlations come from Tornquist et al. (2024) where these parameters were studied per subsection from 2003 to 2018.

For El Niño, Fig. 10 indicates that an increase in southerly winds in S3 during October and February, combined with a rise in SST anomalies in S2 and S3 in April, explains the Chl anomalies observed in these subsections during those months. Furthermore, S3 experienced a decrease in precipitation in April and May which correspond with the rise in Chl levels. It is interesting to note that the Chl anomalies were not as high in the remaining months. The increase in Chl observed in N1-N2 from October to November was not caused by upwelling, considering the significant SST anomaly increments observed there. However, substantial southerly winds appeared in N2 and N3 in November, which did not enhance the Chl anomalies observed by upwelling. These winds were also present in the previous month but were not as strong. The Chl rise in N1 observed from October to February occurred despite the unfavourable upwelling SST conditions experienced there, but with some upwelling-inducing winds in December. Chl drops were also observed in the Peruvian Zone in the same months. These were consistent with the SST anomaly increase in that section. From January through the rest of the seasonal cycle, there was a general Chl anomaly decrease in the Central and part of the Northern Zone. This is compatible with the rise of SST and easterly wind anomalies appearing there.

There were not many substantial physical anomalies during La Niña, unlike El Niño (Fig. 11). However, some favourable conditions still increased productivity and caused local Chl increases. The decrease in

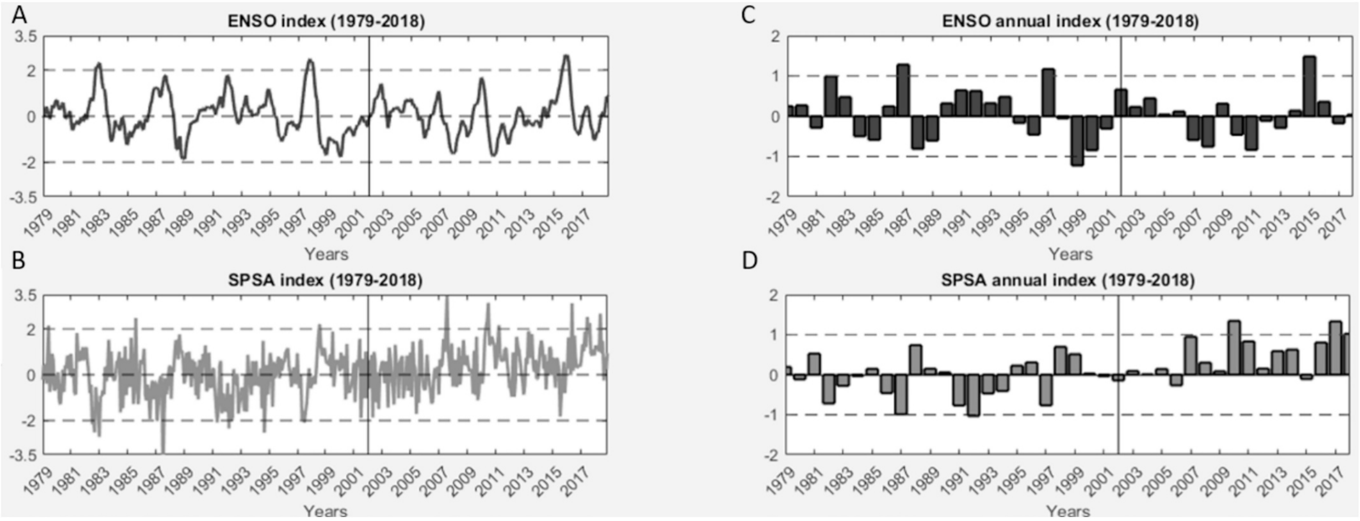

Fig. 7. Time series of ENSO and SPSA indices sampled on both monthly (AB) and annual (CD) scales. A vertical line shows from when the Chl data is available. The scale is normalised to 1.0 SD.

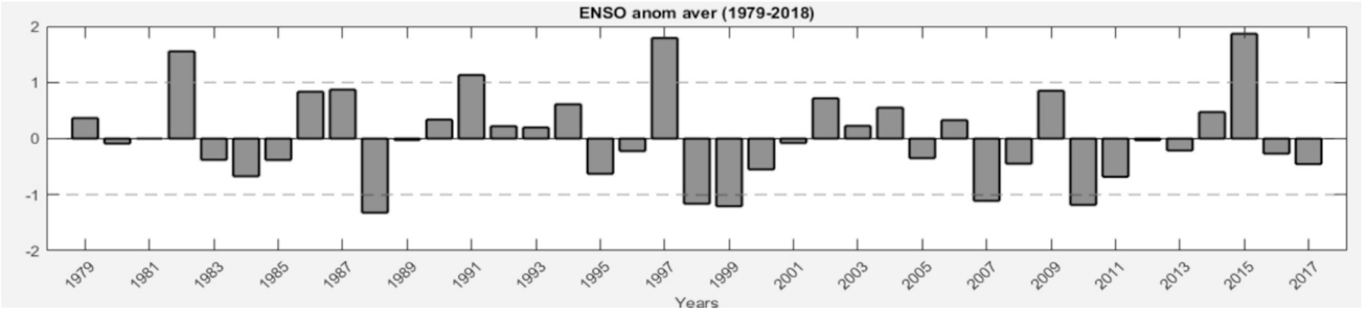

Fig. 8. ENSO annual index (June to May), where the dashed lines represent the limits that were set to create the composites. The scale is normalised to 1.0 SD.

Chl experienced in N1 and N2 from June to October did not match the Southerly winds detected in July in both subsections, nor did it match the N1 drop in SST and rise in precipitation in October. However, the SST drop in December and southerly wind anomalies in March coincided with a Chl increment observed in N1. The westerly wind detected in N2 in May was consistent with the Chl drop there. The decrease experienced in N3 and C1 in July and August corresponds to westerly winds in those subsections. A slight Chl rise in C3 in August, December and April was related to the SST drop experienced in that area, except for April, which was caused by a southerly wind anomaly. In that same month, a slight Chl rise in C1 and C2 is consistent with the decrease in SST anomalies. In the Southern Zone, the S1 behaviour cannot be attributed to any physical parameter anomaly over 1, but minor southerly wind anomalies were observed there in some months. In contrast, unfavourable wind conditions can explain the slight reduction in S2-S3 from December to May. Nonetheless, these conditions were present in December, April and March, when the Chl reductions were higher.

4. Discussion

4.1. Understanding SPSA impacts on phytoplankton productivity

During the El Niño, there was a positive variation in Chl concentration in the Southern Zone during the warm season (section 3.1). This change was caused by an increase in southerly winds and a decrease in PR (section 3.2), which is consistent with the correlations shown in Table 4 between these parameters and Chl. These relationships are explored in detail in Tornquist et al. (2024).

However, in the Central Zone, there was a Chl decrease, which is also in line with the increase in SST and the VW drop. These observations are consistent with the relationship observed in C1 (Figs. 9a, 10a and Table 4). These results follow the findings of Montecinos and Aceituno (2003). Despite a persistent SST rise and modest southerly wind increases, the Northern Zone did not experience important Chl changes. The correlation between these variables was low, which is why N1 was less sensitive to these changes (Table 4).

It has been observed that the phytoplankton productivity on the Chilean coastal region is influenced by the variability of the mentioned physical variables driven by El Niño. Therefore, these changes can be best explained by investigating the likely impacts of ENSO on the SPSA. Essentially, as shown in Fig. 12b, during El Niño warm season, the core of SPSA had lower intensity but expanded towards the south, leading to a slight increase in SLP in the Southern Zone (Fig. 12c). This resulted in substantially decreased westerly winds and PR events during the warm season, while southerly winds increased in September, October, and February.

During La Niña cycles, a slight drop in Chl levels was observed in the Northern and Central Zone from June to October, while the rest of the cycle showed a slight increase (Figs. 9b and 11). However, the Chl in the Northern Zone remained unresponsive to the upwelling-favourable conditions observed in the physical conditions in July (Fig. 11). In the Southern Zone, there was a reduction in Chl levels from December to May due to westerly wind anomalies. Fig. 13b shows a strengthening of SPSA during La Niña, which resulted in almost no variation in the Central and Northern Zone except for some occasional southerly winds, and more intense westerly winds in the Southern Zone Fig. 13c. The only

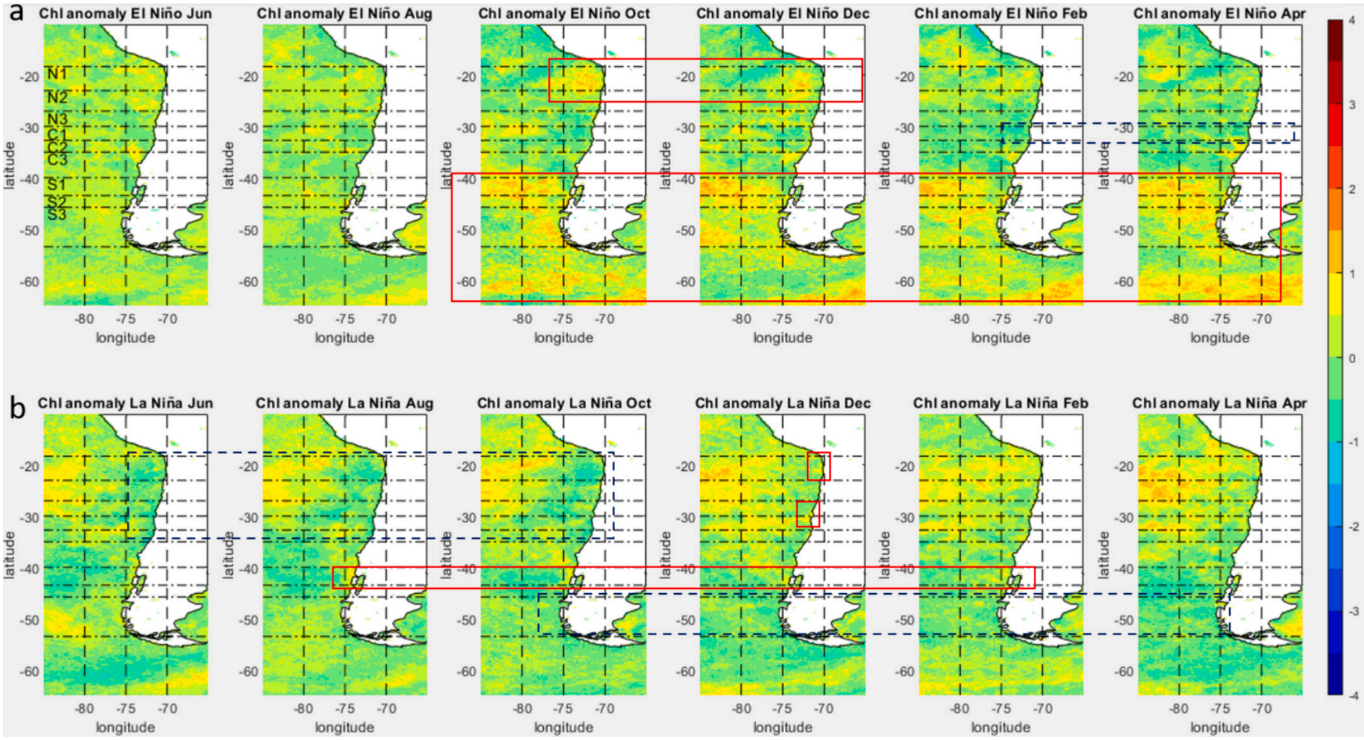

Fig. 9. Annual Chl cycle anomaly normalised composite for El Niño (a) and La Niña (b) showing alternate months. Squares indicate the highest Chl anomalies and dashed squares show the drops.

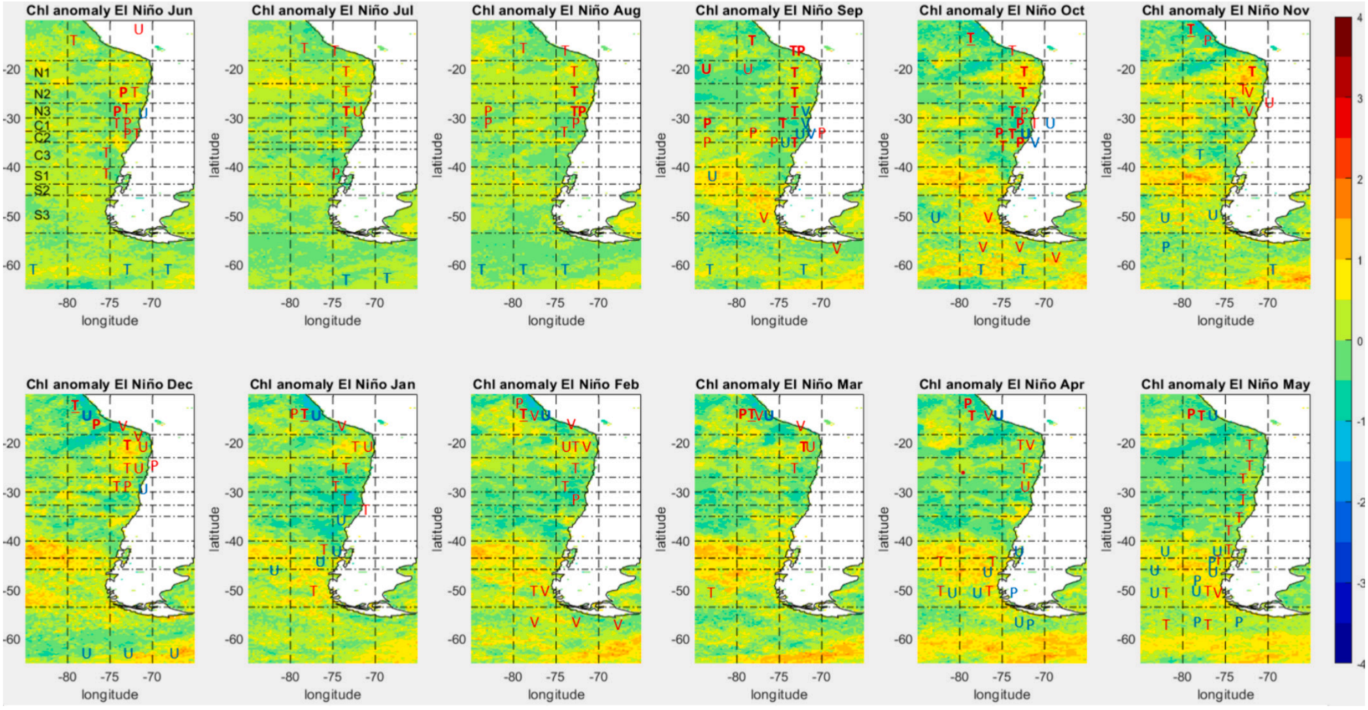

Fig. 10. Schematic showing the physical anomalies normalised over 1 during El Niño where P is PR, T is SST, and U and V are the wind components (UW, VW). The red colour means positive, and blue Negative. The bold terms are between 1 and 1.5, and the bold underlined are beyond 1.5. The dashed vertical lines indicate the subsection limits. These were labelled only in the first panel. The colour bar is the same as in Fig. 9. (For interpretation of the references to colour in this figure legend, the reader is referred to the web version of this article.)

exception was February, where the SLP was lower, reducing the typical southerly winds in S1.

Our findings indicate that the variation in El Niño's Chl anomaly observed in time and space (Fig. 9a) are consistent with the temporal and spatial variations of physical parameters driven by El Niño (Fig. 10), which alter the SPSA (Fig. 12b). The Chl impact during El Niño was mainly in the Southern Zone during the warm season, which was also found by Ancapichun and Garcés-Vargas (2015) and Montecinos and

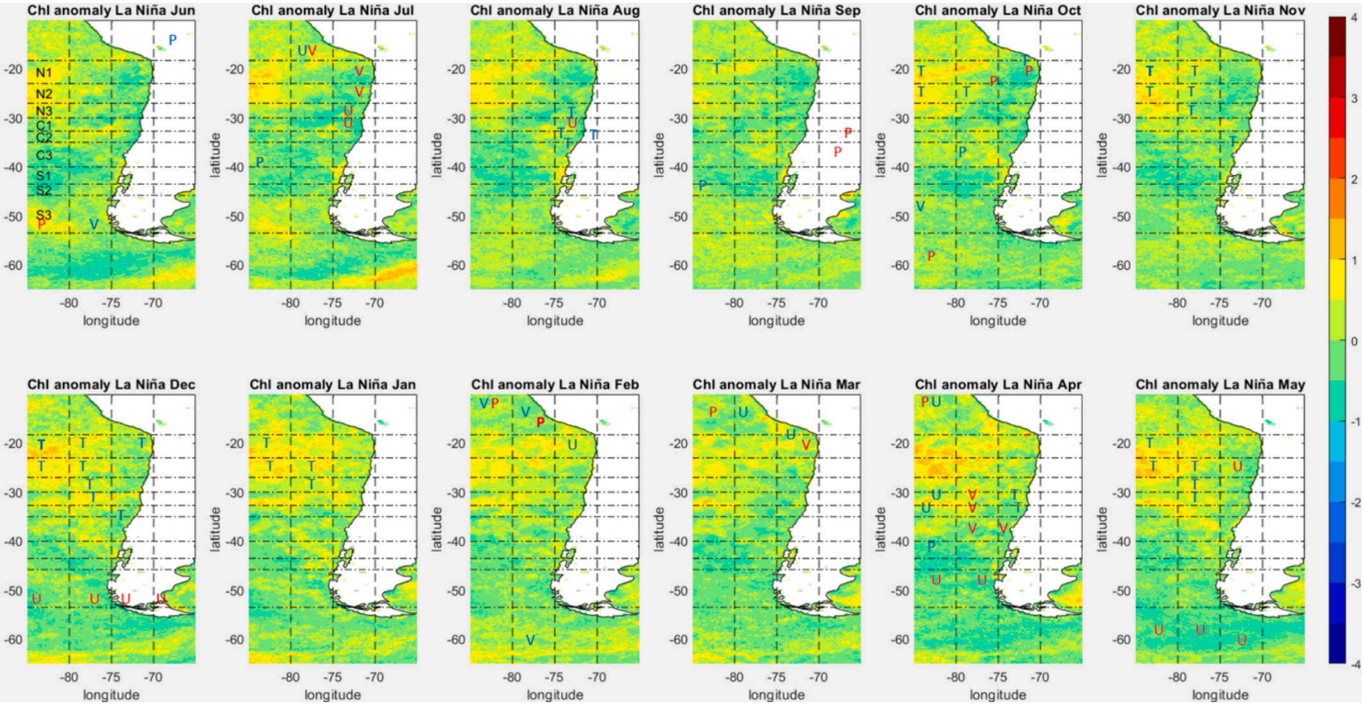

Fig. 11. Schematic showing the physical anomalies anomalies normalised over 1 during La Niña; See Fig. 10 for a full explanation.

Table 4
Chl correlation with the physical parameters per subsection in the coastal strip, the statistically significant correlations are marked with an asterisk ($0.01 < P$-values<0.05), and the statistically very significant are in bold (P-values<0.01; Tornquist et al., 2024).

Rho	Chl ~ SST	Chl ~ PR	Chl ~ VW	Chl ~ UW
N1	−0.10	0.14	0.07	−0.12
N2	−0.13	0.05	0.09	−0.03
N3	−0.12	−0.08	**0.21**	0.10
C1	*−0.16**	−0.07	**0.20**	−0.03
C2	−0.15*	0.04	0.08	0.06
C3	**−0.20**	**−0.33**	**0.38**	**−0.27**
S1	−0.06	**−0.39**	**0.45**	**−0.41**
S2	0.15*	**−0.24**	**0.26**	**−0.29**
S3	**0.20**	**−0.20**	**0.23**	**−0.32**

Aceituno (2003). In contrast, the Northern Zone experienced an increase in SST and at times, more southerly winds, which did not lead to an increase in Chl concentration. This is likely due to the deepening of the thermocline and nutricline as reported by Barber and Chavez (1983), Calienes (2014) and Echevin et al. (2014).

Despite La Niña producing an SPSA reinforcement, this did not lead to longshore wind increments (Figs. 11 and 13), except for a few occasions in the Central and part of the Northern Zone that did not significantly increase the Chl level. However, Gómez et al. (2012) found a notorious Chl increase in C3 during La Niña's Spring. On the other hand, the concentration of the Chl in the Northern Zone is consistent with a low response observed by Tornquist et al. (2024) and the reduced coastal winds reported by Enfield (1981), Kessler (2006), Chamorro et al. (2018) and Huyer et al. (1987). The reason behind this is discussed by Tornquist et al. (2024), indicating that weak winds and narrow coastal shelves in N2 and N3 interfere with the nutrient renovation process.

4.2. *Limitations and considerations*

The remote sensing data comes with uncertainties, especially the Chl algorithm. This algorithm faces difficulty in shallow regions where phytoplankton is present, as noted by Yang et al. (2018) and Abbas et al. (2019). However, this paper aims to estimate general tendencies with substantial changes despite these uncertainties. These are even higher considering the Chl was extended using CCA with a MAE ranging from 0.63 to 0.73 for a variable whose coastal values generally did not exceed ±2 (section 3.2). However, the general tendency of the results was acceptable, given the complexity and high variation that Chl has onshore. The error was minimised using actual and predicted data in the Chl composite construction using 25 % of real data for El Niño and 40 % for La Niña. Despite this, the Chl patterns were consistent with the meteorological composites.

The reconstruction of the Chl time series from SST observations can potentially introduce artificial correlations between SST and Chl. While SST is a valuable predictor for Chl variations, relying heavily on SST data to estimate Chl can lead to an overestimation of the SST-Chl relationship. This is because the algorithm may prioritise SST changes over other factors key to Chl complexity behaviour, such as nutrient availability and light conditions. As a result, caution is needed when interpreting Chl variations derived from SST, as the observed patterns may reflect an enhanced or biased relationship that does not fully represent the underlying ecological dynamics.

The accuracy of the Chl prediction could have been improved by incorporating a second independent variable and utilising SeaWiFS data. Schollaert Uz et al. (2017) made these improvements using SST and bathymetry data to reconstruct the Chl in the tropical Pacific, leading to better predictions. Nevertheless, these were not considered in this study since SeaWiFS and MODIS-Aqua data were only available individually due to maintenance of the merged version. Although, these data sets could have been combined manually, it would have been complex and required significant effort because they have different time and space scales. Additionally, the inclusion of bathymetry as a second variable for feeding the model was not considered due to the challenges in accessing detailed bathymetry data along the Chilean coast and the complexity of the model itself.

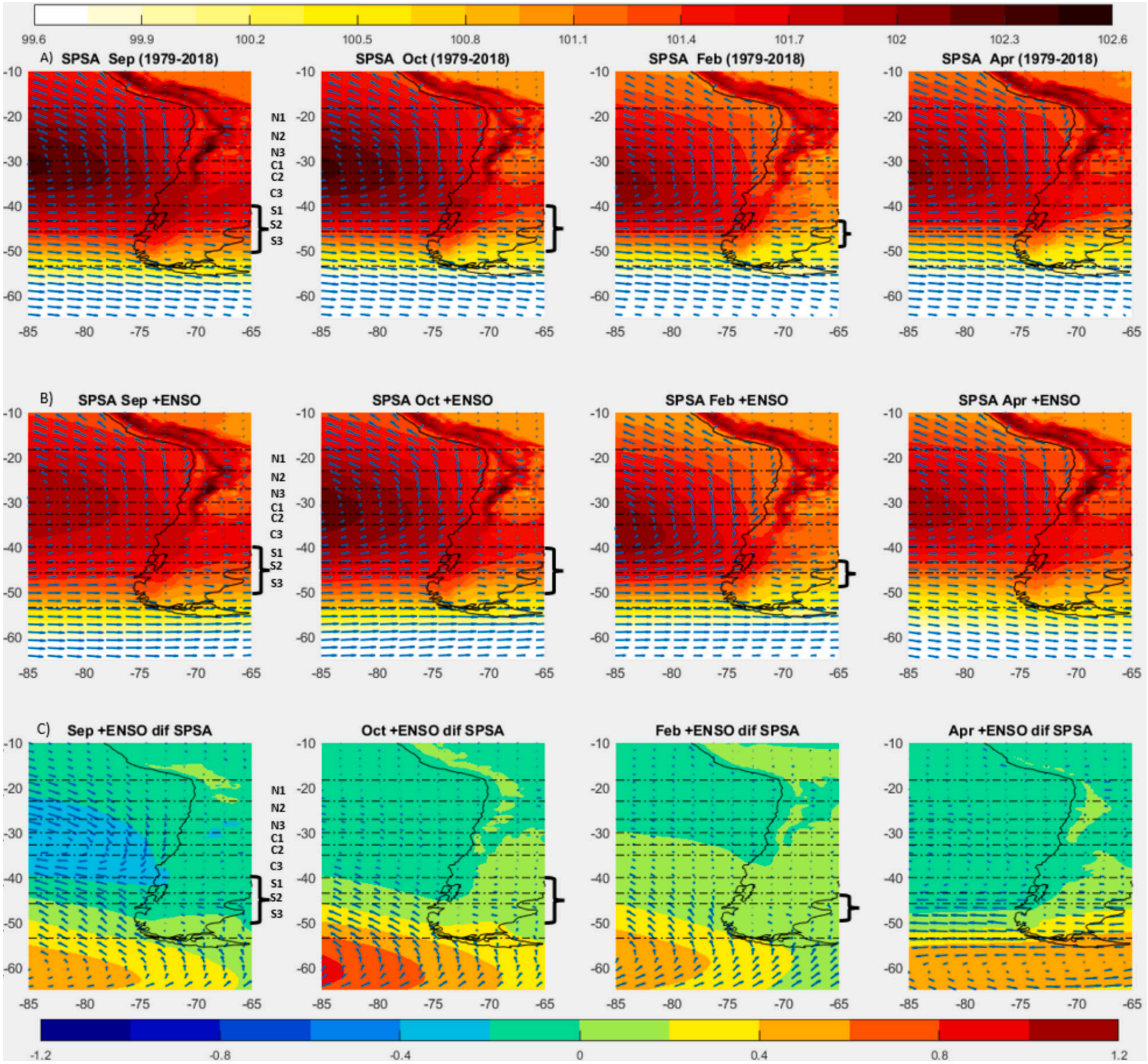

Fig. 12. A) SPSA averaged behaviour for September, October, February and April, where the horizontal lines define each Subsection limit (top colour bar). B) SPSA averaged behaviour in El Niño years (2015, 1997, 1981 and 1991) for the same months (top colour bar). C) El Niño SPSA difference from the regular SPSA (bottom colour bar). The curly brackets indicate the sections where the southerly winds are more substantial than in a regular SPSA year. The C section showed how the SLP was higher in the extreme south. it also exhibited how the westerly winds were weaker during an El Niño year.

5. Conclusions

The use of CCA has proven to be a powerful tool in expanding the Chl variable. This methodology has consistently produced coherent results that align with the observed patterns in meteorological variables, as depicted in Fig. 10 and Ancapichun and Garcés-Vargas (2015) along with Montecino & Aceituno's (2003) findings. Despite the acknowledged uncertainties, this approach has provided valuable insights into the intricate relationship within this dynamic system.

The ENSO composites were useful to determine the spatial and temporal variation of the physical parameters and the Chl. This allowed us to establish the relationship between them and determine which Zones were more affected.

ENSO events induce alterations in the SPSA, leading to shifts in typical winds and precipitation, which affect phytoplankton production. Figs. 12 and 13 highlight that the Southern Zone is more susceptible to these climate variations, while the Northern Zone is almost not affected.

The most relevant change was observed in the Southern Zone (S2 and S3), which experienced a reduction in westerly winds and precipitation, coupled with a slight increase in the southerly winds during warm seasons driven by an SLP-positive variation (Fig. 12). This resulted in a notable boost in phytoplankton production, particularly during strong El Niño episodes. Meanwhile, the Northern Zone showed no noticeable variations in chlorophyll during La Niña and some increases during El Niño. However, these variations were not as noticeable because of the generally low chlorophyll variability (Fig. 3 and Table 4 from Tornquist et al., 2024). This was due to weak winds with minimal variation and the narrow coastal shelf (Tornquist et al., 2024; Tornquist, 2023).

This procedure could be extended to analysing other important climate drivers that have an impact on the SPSA and, consequently, the Chilean coast, such as AAO or the Pacific Decadal Oscillation (PDO).

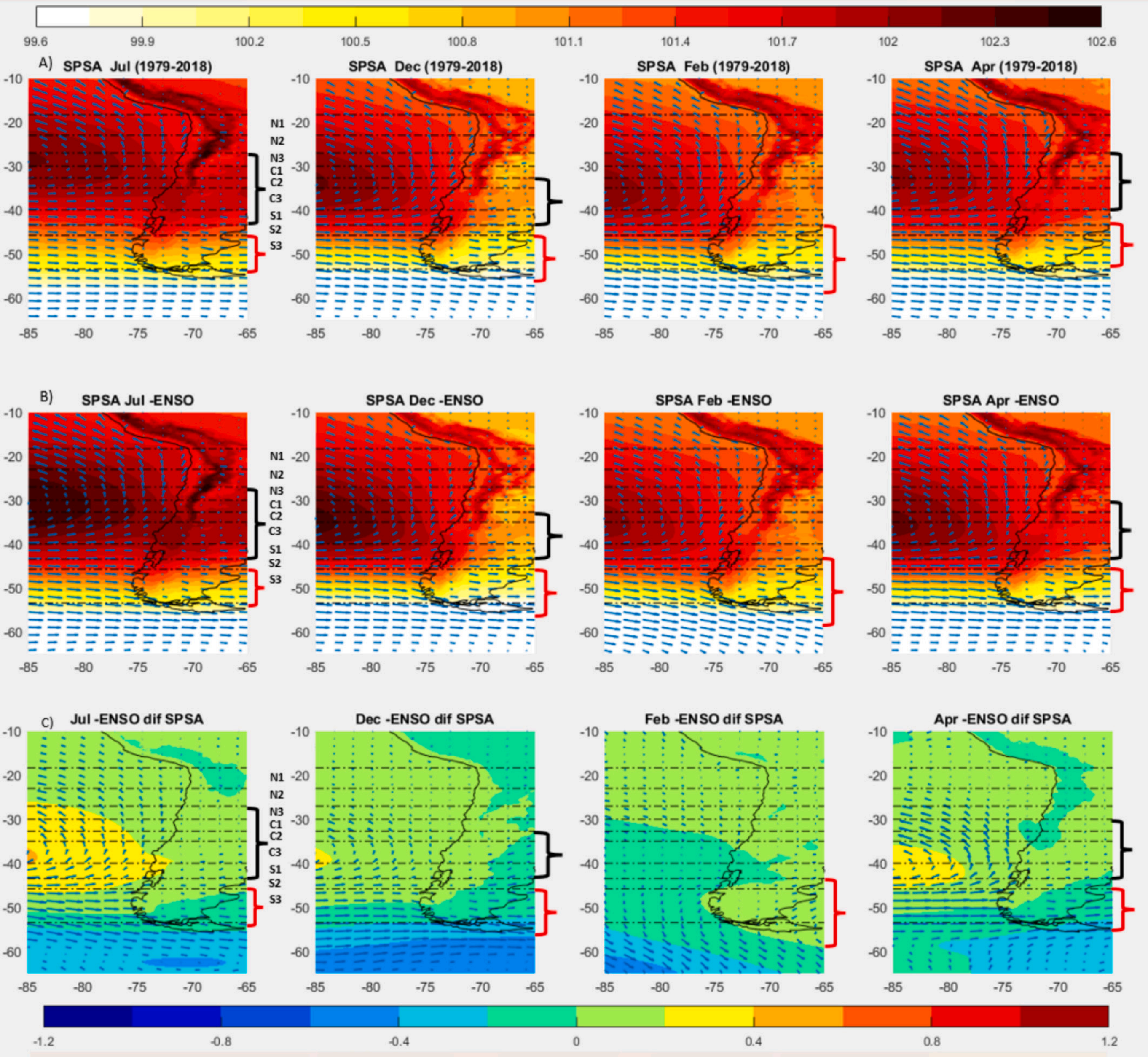

Fig. 13. A) SPSA averaged behaviour for July, December, February and April, where the horizontal lines define each Subsection limit (top colour bar). B) SPSA averaged behaviour in La Niña years (1988, 1999, 2010, 1998 and 2007) for the same months. (top colour bar) C) La Niña SPSA difference from the regular SPSA (bottom colour bar). The black curly brackets indicate the sections where the southerly winds are more substantial than a regular SPSA year, while the red brackets point out when they are lower. The C section showed how the SLP was higher in the central Zone, but it did not noticeable increase the southerly winds. The extreme south displayed lower SLP, leading to downwelling winds. (For interpretation of the references to colour in this figure legend, the reader is referred to the web version of this article.)

CRediT authorship contribution statement

Felipe Tornquist: Writing – original draft, Visualization, Software, Methodology, Investigation, Formal analysis, Data curation. **Grant R. Bigg:** Writing – review & editing, Supervision, Conceptualization. **Robert G. Bryant:** Writing – review & editing, Supervision, Conceptualization.

Declaration of competing interest

The authors declare that they have no known competing financial interests or personal relationships that could have appeared to influence the work reported in this paper.

The authors declare the following financial interests/personal relationships which may be considered as potential competing interests:

Felipe Tornquist reports financial support was provided by Becas Chile, aka ANID.

Data availability

Data will be made available on request.

Acknowledgements

F. Tornquist would like to express gratitude to the Chilean National Agency for Research and Development (ANID) for providing financial support through the DOCTORADO BECAS CHILE/2017- 72180209 scholarship program. We would also like to acknowledge GIOVANNI, NOAA and Copernicus for providing the data used in this study. Special thanks go to Dr. Marc Taylor for sharing his CCA code in his blog, Jose Vicencio Veloso for providing the SPSA index, and, finally, to Paola Bravo and Matias Tornquist for their support.

References

Abbas, M.M., Melesse, A.M., Scinto, L.J., Rehage, J.S., 2019. Satellite estimation of chlorophyll-a using moderate resolution imaging spectroradiometer (MODIS) sensor in shallow coastal water bodies: validation and improvement. Water 11 (8), 1621.

Aguirre, C., Flores-Aqueveque, V., Vilches, P., Vásquez, A., Rutllant, J.A., Garreaud, R., 2021. Recent changes in the low-level jet along the subtropical west coast of South America. Atmosphere 12 (4), 465. https://doi.org/10.3390/atmos12040465.

Ancapichun, S., Garcés-Vargas, J., 2015. Variability of the Southeast Pacific subtropical anticyclone and its impact on sea surface temperature off north-Central Chile. Cienc. Mar. 41 (1), 1–20. https://doi.org/10.7773/cm.v41i1.2338.

Barber, R.T., Chavez, F.P., 1983. Biological consequences of El Niño. Science 222 (4629), 1203–1210.

Barnett, T., Preisendorfer, R., 1987. Origins and levels of monthly and seasonal forecast skill for United States surface air temperatures determined by canonical correlation analysis. Mon. Weather Rev. 115, 1825–1850.

Barrett, B.S., Garreaud, R.D., Falvey, M., 2009. Effect of the Andes cordillera on precipitation from a midlatitude cold front. Mon. Weather Rev. 137 (9), 3092–3109. https://doi.org/10.1175/2009MWR2881.1.

Beckers, J., Rixen, M., 2003. EOF calculations and data filling from incomplete oceanographic datasets*. J. Atmos. Ocean. Technol. 20 (12), 1839–1856.

Bigg, G., 2003. The Oceans and Climate, Second ed. Cambridge University Press. https://doi.org/10.1017/cbo9781139165013.

C3S, 2021. ERA5: Fifth Generation of ECMWF Atmospheric Reanalyses of the Global Climate. Copernicus Climate Change Service Climate Data store. https://cds.climate.copernicus.eu/cdsapp.

Calienes, R., 2014. Producción primaria en el ambiente marino en el Pacifico sudeste. Perú 1960–2000.

Chamorro, A., Echevin, V., Colas, F., Oerder, V., Tam, J., Quispe, Ccalluari C., 2018. Mechanisms of the intensification of the upwelling-favorable winds during El Niño 1997-1998 in the Peruvian upwelling system. Clim. Dyn. 51, 3717–3733.

CONAMA, 2008. Biodiversidad de Chile, Patrimonio y Desafíos (second ed.), Tomo I. https://www.academia.edu/28661207/BIODIVERSIDAD_DE_CHILE_PATRIMONIO_Y_DESAFÍOS_TRADICIONES_CULTURALES_Y_BIODIVERSIDAD.

Cordero, R.R., Asencio, V., Feron, S., Damiani, A., Llanillo, P.J., Sepulveda, E., Jorquera, J., Carrasco, J., Casassa, G., 2019. Dry-season snow cover losses in the Andes (18°–40°S) driven by changes in large-scale climate modes. Sci. Rep. 9 (1) https://doi.org/10.1038/s41598-019-53486-7, 16945–16910.

Echevin, V., Albert, A., Lévy, M., Graco, M., Aumont, O., Piétri, A., Garric, G., 2014. Intraseasonal variability of nearshore productivity in the northern Humboldt current system: the role of coastal trapped waves. Cont. Shelf Res. 73, 14–30. https://doi.org/10.1016/j.csr.2013.11.015.

Enfield, D., 1981. Thermally driven wind variability in the planetary boundary layer above Lima, Peru. J. Geophys. Res. Oceans 86 (C3), 2005–2016.

Espinoza-Morriberón, D., Echevin, V., Colas, F., Tam, J., Ledesma, J., Vásquez, L., Graco, M., 2017. Impacts of El Niño events on the Peruvian upwelling system productivity. J. Geophys. Res. Oceans 122 (7), 5423–5444.

Franz, Werdell, P.J., Meister, G., Bailey, S.W., Epleejr, R.E., Feldman, G.C., Kwiatkowskaa, E., McClain, C., Patt, F., Thomas, D., 2005. The continuity of ocean color measurements from SeaWiFS to MODIS, Vol. 5882, pp. 58820W–58820W-58813.

Friederichs, P., Hense, A., 2003. Statistical inference in canonical correlation analyses exemplified by the influence of North Atlantic SST on European climate. J. Clim. 16 (3), 522–534. https://doi.org/10.1175/1520-0442(2003)016<0522:SIICCA>2.0.CO;2.

Garreaud, R.D., Muñoz, R.C., 2005. The low-level jet off the west coast of subtropical South America: structure and variability. Mon. Weather Rev. 133 (8), 2246–2261. https://doi.org/10.1175/MWR2972.1.

Garreaud, R.D., Boisier, J.P., Rondanelli, R., Montecinos, A., Sepúlveda, H.H., Veloso-Aguila, D., 2020. The Central Chile mega drought (2010–2018): A climate dynamics perspective. Int. J. Climatol. 40 (1), 421–439. https://doi.org/10.1002/joc.6219.

Gómez, F., Montecinos, A., Hormazabal, S., Cubillos, L.A., Correa-Ramirez, M., Chavez, F.P., 2012. Impact of spring upwelling variability off southern-Central Chile on common sardine (Strangomera bentincki) recruitment. Fish. Oceanogr. 21 (6), 405–414. https://doi.org/10.1111/j.1365-2419.2012.00632.x.

Gómez, F.A., Spitz, Y.H., Batchelder, H.P., Correa-Ramirez, M.A., 2017. Intraseasonal patterns in coastal plankton biomass off Central Chile derived from satellite observations and a biochemical model. J. Mar. Syst. 174 (C), 106–118. https://doi.org/10.1016/j.jmarsys.2017.05.003.

Graco, M., Correa Chilon, D., García Díaz, W., Sarmiento, M., 2016. Impactos del ENSO en la biogeoquímica del sistema de afloramiento frente a Perú central, febrero 2013-diciembre 2015.

Hersbach, H., Bell, B., Berrisford, P., Hirahara, S., Horányi, A., Muñoz-Sabater, J., Nicolas, J., Peubey, X., Balsamo, G., Bechtold, P., Biavati, G., Bidlot, J., Bonavita, M., Chiara, G., Dahlgren, P., Dee, D., Diamantakis, M., Dragani, R., Flemming, J., Forbes, R., Fuentes, M., Geer, A., Haimberger, L., Healy, S., Hogan, R., Hólm, E., Janisková, M., Keeley, S., Laloyaux, P., Lopez, P., Lupu, C., Radnoti, G., Rosnay, P., Rozum, I., Vamborg, F., Villaume, S., Thépaut, J.N., 2020. The ERA5 global reanalysis. Q. J. R. Meteorol. Soc. 146 (730), 1999–2049. https://doi.org/10.1002/qj.3803.

Huyer, A., Smith, R.L., Paluszkiewicz, T., 1987. Coastal upwelling off Peru during normal and El Niño times, 1981-1984. J. Geophys. Res. Oceans 92 (C13), 14297–14307.

Kessler, W.S., 2006. The circulation of the eastern tropical pacific: A review. Prog. Oceanogr. 69 (2–4), 181–217.

Mogollón, R., Calil, P.H.R., 2017. On the effects of ENSO on ocean biogeochemistry in the northern Humboldt current system (NHCS): A modeling study. J. Mar. Syst. 172, 137–159. https://doi.org/10.1016/j.jmarsys.2017.03.011.

Montecinos, A., Aceituno, P., 2003. Seasonality of the ENSO-related rainfall variability in Central Chile and associated circulation anomalies. J. Clim. 16 (2), 281–296. https://doi.org/10.1175/1520-0442(2003)016<0281:SOTERR>2.0.CO;2.

NOAA, 2019. Teleconnections. https://www.ncdc.noaa.gov/teleconnections/.

Quintana, J.M., Aceituno, P., 2011. Changes in the rainfall regime along the extratropical west coast of South America (Chile): 30-43° S. Atmosfera 25 (1), 1–22.

Rahn, D.A., 2012. Influence of large scale oscillations on upwelling-favorable coastal wind off Central Chile. J. Geophys. Res. Atmos. 117 (D19) https://doi.org/10.1029/2012JD018016 n/a-n/a.

Saldías, G.S., Largier, J.L., Mendes, R., Pérez-Santos, I., Vargas, C.A., Sobarzo, M., 2016. Satellite-measured interannual variability of turbid river plumes off Central-Southern Chile: spatial patterns and the influence of climate variability. Prog. Oceanogr. 146, 212–222. https://doi.org/10.1016/j.pocean.2016.07.007.

Salvatteci, R., Field, D., Gutiérrez, D., Baumgartner, T., Ferreira, V., Ortlieb, L., Sifeddine, A., Grados, D., Bertrand, A., 2018. Multifarious anchovy and sardine regimes in the Humboldt current system during the last 150 years. Glob. Chang. Biol. 24 (3), 1055–1068. https://doi.org/10.1111/gcb.13991.

Schollaert Uz, S., Busalacchib, A.J., Smith, T.M., Evans, M.N., Brown, C.W., Hackert, E. C., 2017. Interannual and decadal variability in tropical Pacific chlorophyll from a statistical reconstruction: 1958-2008. J. Clim. 30 (18), 7293–7315. https://doi.org/10.1175/JCLI-D-16-0202.1.

Schulz, N., Boisier, J.P., Aceituno, P., 2012. Climate change along the arid coast of northern Chile. Int. J. Climatol. 32 (12), 1803–1814. https://doi.org/10.1002/joc.2395.

Tang, G., Clark, M.P., Papalexiou, S.M., Ma, Z., Hong, Y., 2020. Have satellite precipitation products improved over the last two decades? A comprehensive comparison of GPM IMERG with nine satellite and reanalysis datasets. Remote Sens. Environ. 240, 111697 https://doi.org/10.1016/j.rse.2020.111697.

Taylor, M., 2012. Canonical Correlation Analysis for Finding Patterns in Coupled Fields. Me Nugget. https://menugget.blogspot.com/2012/03/canonical-correlation-analysis-for.html.

Taylor, M., 2017. Sinkr: Collection of functions with Emphasis in Multivariate Data Analysis. https://github.com/marchtaylor/sinkr.

Taylor, M., Losch, M., Wenzel, M., Schröter, J., 2013. On the sensitivity of Field reconstruction and prediction using empirical orthogonal functions derived from Gappy data. J. Clim. 26 (22), 9194–9205. https://doi.org/10.1175/JCLI-D-13-00089.1.

Thiel, M., Macaya, E., Acuna, E., Arntz, W., Bastias, H., Brokordt, K., Camus, P., Carlos Castilla, J., Castro, L., Cortes, M., Dumont, C., Escribano, R., Fernandez, M., Gajardo, J., Gaymer, C., Gómez, I., Gonzalez, A., González, H., Haye, P., Alonso Vega, J., 2007. The Humboldt current system of northern and Central Chile. In: Oceanographic Processes, Ecological Interaction and Socioeconomic Feedback (Vol. 45, pp. 195-344). Oceanography and Marine Biology: An Annual Review.

Tornquist, F., 2023. Examining the Climate Drivers of Phytoplankton Variation along the Chilean Coast. University of Sheffield.

Tornquist, F., Bigg, G., Bryant, R., 2024. Physical mechanisms affecting phytoplankton variability along the Chilean coast. J. Mar. Syst. 242, 103934.

Trenberth, K., 2020. The Climate Data Guide: Nino SST Indices (Nino 1+2, 3, 3.4, 4; ONI and TNI). https://climatedataguide.ucar.edu/climate-data/nino-sst-indices-nino-12-3-34-4-oni-and-tni.

Vergara, O.A., Echevín, V., Sepúlveda, H.H., Quiñones, R.A., 2017. Controlling factors of the seasonal variability of productivity in the southern Humboldt current system (30–40°S): A biophysical modeling approach. Cont. Shelf Res. 148, 89–103. https://doi.org/10.1016/j.csr.2017.08.013.

Vicencio, J., 2021. SPSA index data [mail].

Vicente-Serrano, S., Aguilar, E., Martínez, R., Martín-Hernández, N., Azorin-Molina, C., Sanchez-Lorenzo, A., El Kenawy, A., Tomás-Burguera, M., Moran-Tejeda, E., López-Moreno, J., Revuelto, J., Beguería, S., Nieto, J., Drumond, A., Gimeno, L., Nieto, R., 2017. The complex influence of ENSO on droughts in Ecuador. Observ. Theor. Comput. Res. Clim. Syst. 48 (1–2), 405–427. https://doi.org/10.1007/s00382-016-3082-y.

Von Storch, H., Zwiers, F.W., 1999. Statistical Analysis in Climate Research. Cambridge University Press. https://doi.org/10.1017/CBO9780511612336.

Wilks, D.S., 2011. Statistical Methods in the Atmosphere Science, vol. 100. Elsevier Science & Technology. https://doi.org/10.1016/B978-0-12-385022-5.00012-9.

Yang, M.M., Ishizaka, J., Goes, J.I., Gomes, H.d.R., Maúre, E.D.R., Hayashi, M., Katano, T., Fujii, N., Saitoh, K., Mine, T., Yamashita, H., Mizuno, A., 2018. Improved MODIS-aqua chlorophyll-a retrievals in the turbid semi-enclosed Ariake Bay, Japan. Remote Sens. (Basel, Switzerl.) 10 (9), 1335. https://doi.org/10.3390/rs10091335.